JACS
JOURNAL OF THE AMERICAN CHEMICAL SOCIETY
Article
Cite This: J. Am. Chem. Soc. 2019, 141, 12413−12418
pubs.acs.org/JACS

Ultra-High-Temperature Ferromagnetism in Intrinsic Tetrahedral Semiconductors

Chengxi Huang,[†,#] Junsheng Feng,[‡,§,#] Jian Zhou,[∥] Hongjun Xiang,[*,‡,⊥] Kaiming Deng,[†] and Erjun Kan[*,†]

[†]Department of Applied Physics and Institution of Energy and Microstructure, Nanjing University of Science and Technology, Nanjing, Jiangsu 210094, P. R. China

[‡]Key Laboratory of Computational Physical Sciences (Ministry of Education), State Key Laboratory of Surface Physics, and Department of Physics, Fudan University, Shanghai 200433, P. R. China

[§]School of Physics and Materials Engineering, Hefei Normal University, Hefei 230601, P. R. China

[∥]Center for Advancing Materials Performance from the Nanoscale, State Key Laboratory for Mechanical Behavior of Materials, Xi'an Jiaotong University, Xi'an, 710049, China

[⊥]Collaborative Innovation Center of Advanced Microstructures, Nanjing 210093, P. R. China

Supporting Information

ABSTRACT: Ferromagnetic semiconductors exhibit novel spin-dependent optical, electrical, and transport properties, which are promising for next-generation highly functional spintronic devices. However, the possibility of practical applications is hindered by their low Curie temperature. Currently, whether semiconducting ferromagnetism can exist at room temperature is still unclear because of the absence of a solid physical mechanism. Here, on the basis of tight-binding model analysis and first-principles calculations, we report that ferromagnetism in a tetrahedral semiconductor originating from superexchange interactions can be strong enough to survive at room temperature because of the weakening of antiferromagnetic direct-exchange interactions. On the basis of the explored mechanism, a zinc-blende binary transition metal compound, chromium carbide, is predicted to be an intrinsic ferromagnetic tetrahedral semiconductor with a Curie temperature that is as high as ∼1900 K. These findings not only expand the understandings of magnetism in semiconductors but also are of great interest for room-temperature spintronic applications.

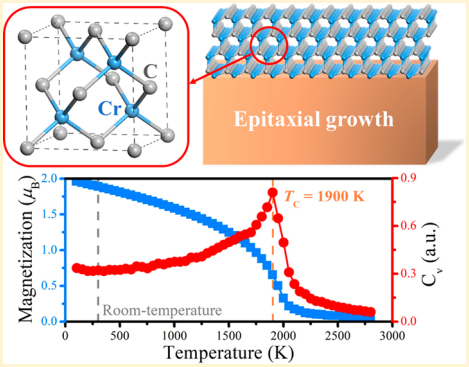

1. INTRODUCTION

Giving both charge and spin degrees of freedom, a material that is simultaneously semiconducting and ferromagnetic (FM) has become one of the most promising candidates for future low-cost, high-performance, multifunctional spintronic applications such as tunneling magnetoresistance sensors, spin field-effect transistors, magnetocapacitors, magnetic random access memories, and quantum computation/communication.[1−4] The most urgent and crucial problem in developing these applications is to search for an FM semiconductor with a Curie temperature (T_C) higher than room temperature. For the past few decades, diluted magnetic semiconductors (DMSs) have received intensive attention as a potential solution. However, despite tremendous effort with respect to DMSs, problems such as rather small net magnetizations, low T_C, uncontrollable magnetic dopant distributions, and ambiguous magnetic phase transitions are difficult to solve.[5,6] On the other hand, intrinsic FM semiconductors that exhibit large and homogeneous spontaneous magnetizations without introducing any magnetic impurities may be another promising route to realizing simultaneously semiconducting behavior and ferromagnetism. Recent great progress on intrinsic FM semiconductors[7−15] has demonstrated the unique advantages and potentials of intrinsic FM semiconductors for novel physics and applications. Unfortunately, the T_C of almost all known intrinsic FM semiconductors is below 130 K,[16−19] preventing any realistic applications. Consequently, it is highly desirable to enhance the T_C of an intrinsic FM semiconductor up to room temperature.[20]

Different from DMSs (e.g., T_C of ∼180 K for Mn-doped GaAs[21]) and magnetic metals/half-metals[22] (e.g., T_C of ∼1100 K for cobalt metal), in the absence of itinerant carriers, the competition between the FM superexchange interactions and the antiferromagnetic (AFM) direct exchange interactions usually leads to weak FM or AFM couplings in an intrinsic semiconductor.[23−25] To enhance T_C, one can either enhance the FM superexchange interactions (e.g., by decreasing the energy difference between the filled and empty d levels[26]) or suppress the AFM direct exchange interactions. To the best of

Received: June 17, 2019
Published: July 16, 2019

DOI: 10.1021/jacs.9b06452
J. Am. Chem. Soc. 2019, 141, 12413−12418

our knowledge, almost all known intrinsic FM semiconductors (e.g., $CrBr_3$, EuO, $CdCr_2S_4$ spinel, and $BiMnO_3$ perovskite) contain octahedrally coordinated magnetic ions. Is it possible to find high-T_C intrinsic FM semiconductors with a different coordination environment for the magnetic ions? We notice that in a tetrahedrally coordinated system [e.g., the zinc-blende (ZB) compound that is compatible with current CMOS technology], (i) the crystal field is much weaker (<50%) than that of an octahedral crystal, which may enhance the FM superexchange interactions; (ii) the number of nearest-neighbor magnetic sites of a given magnetic ion in a ZB compound (12) can be much larger than that in an octahedral crystal (e.g., 6 for a perovskite compound, 4 for a spinel compound, and 3 for a $CrBr_3$-type compound); and (iii) the direct AFM interactions between neighboring magnetic ions may be tuned by a different crystal environment. These facts suggest that it might be possible to enhance the FM couplings in a tetrahedral semiconductor, which motivates us to study the magnetic couplings and seek high-temperature ferromagnetism in intrinsic tetrahedral semiconductors (i.e., ZB semiconductors). In particular, we will investigate whether the AFM direct exchange in the ZB compound can be weaker than that in the octahedral crystals.

In this work, we demonstrated that the T_C of an intrinsic FM semiconductor can be significantly enhanced by weakening the direct-exchange interactions. Our tight-binding model analysis shows that the AFM direct-exchange interactions in a ZB tetrahedral crystal containing magnetic ions with a d^2 electronic configuration are inherently much weaker than that in an octahedral crystal, which may lead to much stronger FM couplings. Through performing extensive first-principles calculations (see section I in the Supporting Information) on possible ZB binary transition-metal compounds, we found that ZB chromium carbide (ZB-CrC) indeed exhibits remarkably strong FM couplings with an estimated T_C that is as high as ~1900 K. Careful analysis of the electronic structures reveals that strong FM couplings in these ZB systems originate from the relatively weak direct interactions between half occupied e orbitals, a weak tetrahedral crystal field, and the strong covalency of metal−ligand bonds, which is consistent with the TB analysis. Film-form ZB-CrC, which maintains robust semiconducting ferromagnetism properties, is further proposed to be synthesizable by the molecular-beam epitaxial (MBE) growth method.

2. RESULTS AND DISCUSSION

2.1. Tight-Binding Analysis for Octahedral and Tetrahedral Crystals. We first adopt a TB cluster model (including two nearest-neighbor magnetic ions) to explore the super- and direct-exchange interactions in a tetrahedral crystal and its difference from those in a common octahedral crystal (section II in the Supporting Information). For conventional octahedral FM semiconductors, such as the $CdCr_2S_4$ spinel and CrI_3, the octahedrons are connected through edge sharing. In this case (Figure 1a), the metal−ligand−metal bonding angle is ~90°, allowing superexchange interactions between half-occupied t_{2g} and empty e_g orbitals, which is responsible for the appearance of FM couplings according to the Good-enough−Kanamori−Anderson (GKA)[23−25] rules of superexchange theory. For a tetrahedral crystal (e.g., the ZB compound), the metal−ligand−metal bonding angle is ~109.5° [the exact value is $\pi - \arcsin(2(\sqrt{2})/3)$] (Figure 1d), which also allows the $t_2 \leftrightarrow p \leftrightarrow e$ superexchange path

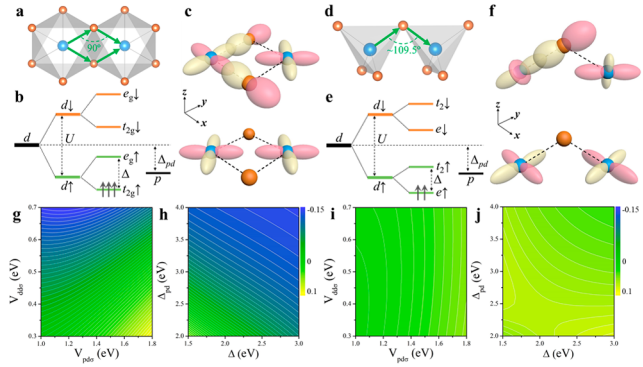

Figure 1. (a) Edge-sharing octahedral and (d) point-sharing tetrahedral cluster models. Blue and orange balls represent magnetic transition-metal ions and nonmagnetic ligand ions, respectively. Green arrows represent the metal−ligand−metal cluster including the nearest-neighbor exchange path. The evolution of d orbitals under (b) octahedral and (e) tetrahedral crystal fields. Atomic-orbital-based schematic diagram of a superexchange path (upper panel) and a direct-exchange path (lower panel) for (c) octahedral and (f) tetrahedral crystals. For octahedral crystals, the presented super-exchange and direct-exchange paths are $d_{x^2-y^2} \leftrightarrow p_x(p_y) \leftrightarrow d_{xy}$ and $d_{xy} \leftrightarrow d_{xy}$, respectively. For tetrahedral crystal, those are $d_\epsilon \leftrightarrow p_\sigma \leftrightarrow d_\gamma$ [$d_\epsilon = \sqrt{3}/3(d_{xy} + d_{yz} + d_{xz})$, $d_\gamma = \sqrt{2}/2(d_{x^2-y^2} + d_{z^2})$ and $p_\sigma = \sqrt{3}/3(p_x + p_y + p_z)$] and $d_{x^2-y^2} \leftrightarrow d_{x^2-y^2}$, respectively. The exchange energy ($E_{ex} = E_{AFM} - E_{FM}$) in eV as a function of the Slater−Koster hopping integrals ($V_{dd\sigma}$ and $V_{pd\sigma}$), the energy-level difference between d and p orbitals (Δ_{pd}), and the energy-level split caused by the crystal field (Δ) for (g and h) octahedral and (i and j) tetrahedral crystals. Blue and yellow colors indicate antiferromagnetic and ferromagnetic coupling, respectively. (g−j) We set $V_{dd\sigma} = -4V_{dd\pi} = -8V_{dd\delta}$, $V_{pd\sigma} = -2.5V_{pd\pi}$, and $U = 3.5$ eV. (g and i) $\Delta = 2$ eV and $\Delta_{pd} = 2.5$ eV. (h and j) $V_{dd\sigma} = -0.7$ eV and $V_{pd\sigma} = -2.0$ eV.

(Figure 1f), thus FM coupling can also be expected. To satisfy the condition of semiconducting, the electron configurations of the magnetic ion for the octahedral and tetrahedral clusters should be t_{2g}^3 and e^2 (Figure 1b,e), respectively. (Without a loss of generality, here we consider the case with less than half-filled d orbitals. In the case with more than half-filled d orbitals, the ferromagnetism is found to be weak. (See section V in the Supporting Information.) Using atomic orbitals (p orbitals of ligands and d orbitals of transition metals) as a basis, we construct the Hamiltonian of the clusters and numerically diagonalize it to investigate the dependence of the exchange energies ($E_{ex} = E_{AFM} - E_{FM}$) on the adjustable parameters such as the Slater−Koster bond integrals[27] ($V_{dd\sigma}$ and $V_{pd\sigma}$, which determine the strength of direct- and superexchange interactions, respectively), the on-site energy level difference between d and p orbitals (Δ_{pd}, which reflects the covalency of metal−ligand bonds), and the crystal field split (Δ, which is also the energy gap between occupied and empty d orbitals near the Fermi level in this case) (Figure 1b,e). (See section II in the Supporting Information for details.)

As shown in Figure 1g−j, E_{ex} for the tetrahedral crystal is generally larger than that for the octahedral crystal when the same parameters are adopted, suggesting that FM couplings in the tetrahedral crystal are inherently stronger. As expected, for both octahedral and tetrahedral crystals, E_{ex} is proportional to $V_{pd\sigma}$ (Figure 1g,i), indicating that the $d \leftrightarrow p \leftrightarrow d$ superexchange that allows effective interactions between t_2 and e orbitals is the origin of FM coupling for both systems (Figure 1c,f). On the other hand, we find that E_{ex} increases as Δ and Δ_{pd} decrease (Figure 1h,j), in agreement with our

DOI: 10.1021/jacs.9b06452
J. Am. Chem. Soc. 2019, 141, 12413−12418

previous work.[26] This can be understood: Reducing Δ will strengthen the $t_2 \leftrightarrow e$ interactions, and reducing Δ_{pd} will strengthen the $d \leftrightarrow p$ interactions, which both favor FM couplings.

Next we look into the direct-exchange interactions. For the octahedral crystal, E_{ex} rapidly decreases with the increase in $V_{dd\sigma}$ (Figure 1g), indicating that the $d \leftrightarrow d$ direct-exchange prefers AFM, which competes with the superexchange interactions, and the influence of $d \leftrightarrow d$ direct exchange on the magnetic couplings is remarkable. When the $d \leftrightarrow d$ direct exchange is strong enough, the system even becomes AFM. However, for the tetrahedral crystal, we find that E_{ex} barely changes with $V_{dd\sigma}$ (Figure 1i), which is quite surprising and interesting. In the octahedral crystal, the lower $t_{2g}\uparrow$ orbitals are occupied and the higher $e\uparrow$ orbitals are empty. Thus, the AFM direct exchange is mainly contributed by the $t_{2g} \leftrightarrow t_{2g}$ (e.g., $d_{xy} \leftrightarrow d_{xy}$ shown in Figure 1c) interaction. While in the tetrahedral crystal, the $t_2\uparrow$ and $e\uparrow$ orbitals are reversed and the AFM direct exchange is dominated by the $e \leftrightarrow e$ (e.g., $d_{x^2-y^2} \leftrightarrow d_{x^2-y^2}$ shown in Figure 1f) interaction. From the Hamiltonian matrix of $d \leftrightarrow d$ direct exchange for the clusters, we find that the $d_{xy} \leftrightarrow d_{xy}$ hopping term is $(V_{dd\delta} + 3V_{dd\sigma})/4$ and the $d_{x^2-y^2} \leftrightarrow d_{x^2-y^2}$ hopping term is $V_{dd\pi}$. Because $|V_{dd\sigma}|$ is usually much larger than $|V_{dd\pi}|$ and $|V_{dd\delta}|$ (more than 4 times) in a transition-metal compound,[28] the $e \leftrightarrow e$ ($d_{x^2-y^2} \leftrightarrow d_{x^2-y^2}$) interaction is always expected to be much weaker than the $t_2 \leftrightarrow t_2$ ($d_{xy} \leftrightarrow d_{xy}$) interaction. This can also be understood by examining the distribution of the e orbitals (Figure 1f). Thus, the AFM direct exchange in a tetrahedral crystal is demonstrated, for the first time, to be much weaker than that in an octahedral crystal, which is independent of material compositions and is a general mechanism for tetrahedral crystals. (A detailed analytical derivation is presented in section II in the Supporting Information.)

2.2. Zinc-Blende Ferromagnetic Semiconductors. Overall, our TB analysis proposes that a tetrahedral semiconductor can display much stronger FM couplings than an octahedral semiconductor. To prove this idea and search for possible high-temperature intrinsic FM semiconductors in real tetrahedral crystals, a series of ZB binary transition-metal compounds, denoted as ZB-MXs (transition metal M = Sc−Ni, Zr−Rh, Hf−Ir and ligand X = C, Si, N, P, O, S, and Se), were systematically investigated by extensive first-principles calculations. We note that some of these ZB-MXs have been previously predicted to be metals or half-metals,[29,30] and it was claimed that ZB-VAs exhibit semiconductor-like behavior.[29] But the origin of magnetic couplings were not well explored, and a sizable electronic band gap was not clearly observed. Thus, here we focus on the ZB-MXs semiconductors with a sizable electronic band gap, where the ferromagnetic couplings should be dominated by superexchange interactions. Table S3 in the Supporting Information lists the predicted FM semiconducting ZB-MXs. (Discussions of other considered ZB-MXs and wurtzite-MXs are presented in section V in the Supporting Information.) Interestingly, among them, the ZB-CrC possesses a sizable electronic band gap (0.69 eV) and a rather strong FM coupling with a T_C of as high as ∼1900 K (the calculation of T_C is discussed in the following), much beyond room temperature and higher than the conventional octahedral FM semiconductor (e.g., ∼90 K for $CdCr_2S_4$[18] and ∼61 K for CrI_3[31]). In the following text, we focus on ZB-CrC to explore the electronic and magnetic properties of the ZB FM semiconductors.

2.3. Electronic and Magnetic Properties of Zinc-Blende CrC. Figure 2a shows the ZB structure of CrC (space

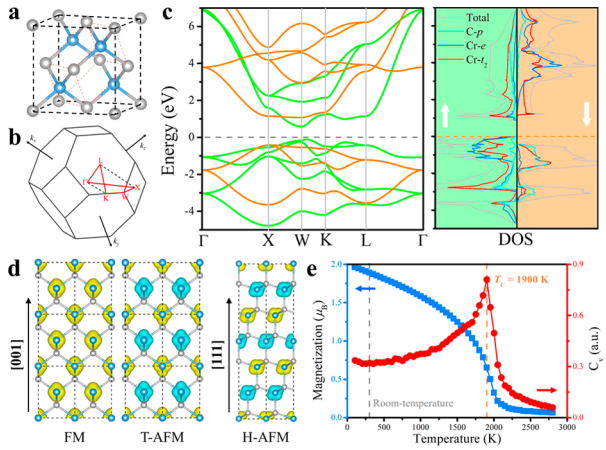

Figure 2. (a) Conventional cell and primitive cell of the ZB-CrC and other ZB binary transition-metal compounds. Blue and gray balls represent the transition metal and ligand ions, respectively. (b) Brillouin zone and high symmetric path for ZB compounds. (c) Spin-polarized band structure and density of states for ZB-CrC. Green and orange lines (regions) represent spin-up and spin-down bands (channels), respectively. (d) Spatial spin density of FM, T-AFM, and H-AFM configurations. Yellow and cyan isosurfaces represent the net spin-up and spin-down charges, respectively. [001] and [111] represent the crystal orientation of the conventional cell. (e) Average magnetization per Cr and specific heat (C_v) as functions of temperature from Monte Carlo simulations.

group $F\bar{4}3m$). Each Cr is tetrahedrally coordinated by four C ligands, thus the Cr d orbitals split into two parts, namely, the e (d_{z^2} and $d_{x^2-y^2}$) and t_2 (d_{xy}, d_{xz}, and d_{yz}) manifolds. In ZB-CrC, each Cr ion gives four electrons to form bonds with C ions. The left two electrons half occupy the lower e orbitals, and the higher t_2 orbitals are empty, leading to a formal magnetic moment of $2\mu_B$ on each Cr ion. The FM ground state is lower than the T-AFM and H-AFM states by 0.428 and 0.293 eV/Cr, respectively. The spin−orbit coupling (SOC) effect is very small with a magnetic anisotropic energy of less than 0.01 meV (section III in the Supporting Information) and is ignored hereafter.

Figure 2c shows the electronic band structure and density of states (DOS) of ZB-CrC. We can see a large overlap between Cr d and C p orbitals and a large bandwidth (∼12 eV) for the Cr d orbitals, suggesting strong $d \leftrightarrow p$ hybridization. This is due to the small Cr−C bond length (1.96 Å) and small Δ_{pd} (1.5 eV) estimated from the maximally localized Wannier function (MLWF) analysis (Table S2 in the Supporting Information). For comparison, in ZB-TiS, the bandwidth of Ti d orbitals, Ti−S bond length, and Δ_{pd} are ∼5 eV, 2.56 Å, and 4.9 eV, respectively. Furthermore, the Δ value of ZB-CrC is also relatively small (1.6 eV) compared to those of $CdCr_2S_4$ (2.5 eV) and CrI_3 (2.1 eV). These factors are responsible for its strong FM couplings. Overall, the strength of FM couplings for the ZB systems decreases with the increases in their metal−ligand bond length, Δ_{pd} and Δ (Table S2 in the Supporting Information), which is consistent with our TB analysis using the cluster models. It is worth noting that the direct exchange is sensitive to the metal−metal distance. Thus, tensile strain can usually reduce the direct-exchange interactions and enhance the FM couplings, but in ZB-CrC, we find that a

DOI: 10.1021/jacs.9b06452
J. Am. Chem. Soc. 2019, 141, 12413−12418

lattice expansion barely affects the strength of FM couplings (Figure S8 in the Supporting Information), suggesting that the direct-exchange interactions are already rather weak in ZB-CrC and can hardly be further weakened. The large dispersion of the conduction band minimum state near W point (see Figure 2c) suggests that the electron mobility in n-type doped CrC might be high.

Because of the localization of 3d electrons responsible for magnetism, we use the Heisenberg model including NN exchange interactions to describe the magnetic interactions in this system. (See Figure S6 in the Supporting Information for results considering both NN and next-nearest-neighbor exchange interactions.) The spin Hamiltonian reads

$$\hat{H} = -\sum_{\langle ij \rangle} J_1 \vec{S}_i \cdot \vec{S}_j$$

where the summation $\langle ij \rangle$ runs over all of the NN Cr sites. Here we adopt $|\mathbf{S}| = 1$. NN exchange parameter J_1 is calculated to be 53.5 meV, which is more than 4 times larger than that of $CdCr_2S_4$ (13 meV) and CrI_3 (9 meV). As previously mentioned, the number of NN Cr sites for ZB-CrC is as large as 12, which also suggests a high T_C. By performing Metropolis Monte Carlo (MC) simulations (section I in the Supporting Information), the T_C of ZB-CrC is estimated to be ~1900 K. For comparison, the T_C values of the CrI_3 monolayer, $CdCr_2S_4$, and $CdCr_2Se_4$ bulk estimated by the same method are ~50, ~130, and ~150 K (Figure S6 in the Supporting Information), respectively, very close to the experimental values (~45,[8] ~97, and ~142 K,[18] respectively). Note that the high-temperature semiconducting ferromagnetism features of ZB-CrC are independent of the choice of computational methods (i.e., DFT+U, hybrid HSE06, and all-electron functionals; see table S1 in the Supporting Information) and are robust against carrier doping and epitaxial strain (Figures S7 and S9 in the Supporting Information).

2.4. Stability and Experimental Feasibility of Zinc-Blende CrC. Next, we explore the stability and feasibility of ZB-CrC. Its dynamic and thermal stability at 500 K have been examined by phonon calculations and ab initio molecular dynamical simulations (Figure 3b,c and Figure S10 in the Supporting Information), respectively. Global optimizations[32,33] give three low-energy isomers of CrC, namely, the rock-salt (RS, space group $Fm\bar{3}m$), the hexagonal (Hex, space group $P\bar{6}m2$), and the ZB structure (Figure 3a), whose relative energies are 0, 0.522, and 0.518 eV per formula unit, respectively. Similar to most early-transition-metal (e.g., Cr and Mn) binary compounds, CrC also favors RS structure in bulk form. Nevertheless, recent MBE growth experiments report that these binary compounds do show ZB structures in thin-film form on a substrate (e.g., ZB-CrAs on the GaAs substrate[34] and ZB-MnTe on the ZnTe substrate[35]). To find out whether the ZB-CrC film may also be synthesized on a substrate, we examined the relative stability of RS-, Hex-, and ZB-CrC films on two possible substrates, namely, GaN and ZnO wurtzite, which are widely used in the modern semiconductor industry and in surface growth experiments (Figure S13 in the Supporting Information). Our calculations show that, on the (0001) surface of these substrates (GaN and ZnO), a film containing three Cr and C layers indeed favors ZB structures, which are lower in energy than the RS structures by 0.065 and 0.067 eV per Cr. This can be understood as follows: (i) The ZB structure (with a lattice mismatch of ~1.3%) shows better interface matching with the substrate than does the RS structure (with a lattice mismatch of ~9.3%; Figures S11 and S13 in the Supporting Information). (ii) Slight electron doping caused by the substrate can further stabilize the ZB phase against the RS and Hex phases (Figure 3d). In addition, with a large transition barrier (~0.2 eV/Cr) from the ZB to RS phase (Figure S12 in the Supporting Information), the ZB-CrC film is expected to be synthesized by MBE growth on the GaN(0001) or ZnO(0001) surfaces (Figure 3e) and maintain semiconducting and FM features under a high temperature (Figure S13 in the Supporting Information). Interestingly, we further find that even a single ZB-CrC layer can be stable on the 6H-SiC(0001) surface, in which the strong ferromagnetic and semiconducting features are also well preserved, making it a high-temperature two-dimensional ferromagnetic semiconductor (Figure S14 in the Supporting Information)

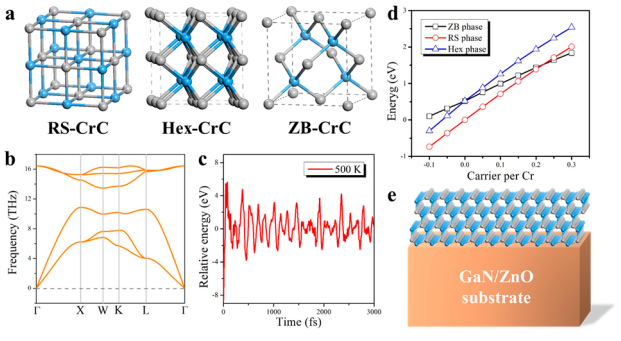

Figure 3. (a) Possible isomers of CrC: rock salt (RS), hexagonal (Hex) and zinc-blende (ZB) structures. (b) Phonon dispersion of ZB-CrC. (c) Ab initio molecular dynamical simulations of ZB-CrC at 500 K. (d) Relative energies of ZB-, RS-, and Hex-CrC as functions of carrier concentration. Negative and positive values of carrier concentration represent hole and electron doping, respectively. (e) Possible substrate for molecular beam epitaxial growth of the ZB-CrC film.

3. CONCLUSIONS

On the basis of a TB cluster model and first-principles calculations, we demonstrate for the first time that ferromagnetism in a tetrahedral semiconductor with d^2 magnetic ions can be much stronger than that in an octahedral one with d^3 magnetic ions. We theoretically design a series of intrinsic high-temperature FM semiconducting tetrahedral crystals, which are compatible with the modern semiconductor industry and existing CMOS technology. Among them, ZB-CrC shows a sizable electronic band gap (0.69 eV) and a T_C of as high as ~1900 K. Such strong FM couplings in these ZB structures may be caused by (1) the weak AFM direct-exchange interactions, (2) the small energy splitting of the tetrahedral crystal field, (3) the strong covalency of metal−ligand bonds, and (4) the large number of nearest-neighbor magnetic sites. Furthermore, a possible approach to achieving the ZB-CrC film, namely, the MBE growth method, is proposed. Our findings not only expand the general knowledge of superexchange theory but also present a new platform for developing room-temperature spintronic applications.

DOI: 10.1021/jacs.9b06452
J. Am. Chem. Soc. 2019, 141, 12413−12418

■ ASSOCIATED CONTENT

Supporting Information

The Supporting Information is available free of charge on the ACS Publications website at DOI: 10.1021/jacs.9b06452.

Details of computational methods, the tight-binding cluster model, electronic and magnetic properties of ZB-CrC, stability and feasibility of ZB-CrC, and properties of other ZB binary transition compounds (PDF)

■ AUTHOR INFORMATION

Corresponding Authors

*E-mail: hxiang@fudan.edu.cn.

*E-mail: ekan@njust.edu.cn.

ORCID

Chengxi Huang: 0000-0003-1491-3954

Jian Zhou: 0000-0002-2606-4833

Hongjun Xiang: 0000-0001-9465-5216

Erjun Kan: 0000-0003-0433-4190

Author Contributions

#These authors contributed equally.

Notes

The authors declare no competing financial interest.

■ ACKNOWLEDGMENTS

Work at NJUST is supported by the NSFC (51522206, 11774173, 11574151, and 51790492) and by PAPD, the Fundamental Research Funds for the Central Universities (no. 30915011203). Work at Fudan is supported by NSFC (11825403), the Special Funds for Major State Basic Research (2015CB921700), Program for Professor of Special Appointment (Eastern Scholar), and Qing Nian Ba Jian Program. J.Z. acknowledges the Youth Thousand Talents Program of China and the Young Talent Support Plan of Xi'an Jiaotong University. C.H. and E.K. acknowledge support from the Tianjing Supercomputer Centre and Shanghai Supercomputer Center. We thank Yongpin Du from NJUST for help with the all-electron DFT calculations.

■ REFERENCES

(1) Fert, A. Nobel Lecture: Origin, development, and future of spintronics. *Rev. Mod. Phys.* **2008**, *80*, 1517.

(2) Wolf, S. A.; Awschalom, D. D.; Buhrman, R. A.; Daughton, J. M.; von Molnár, S.; Roukes, M. L.; Chtchelkanova, A. Y.; Treger, D. M. Spintronics: A Spin-Based Electronics Vision for the Future. *Science* **2001**, *294*, 1488−1495.

(3) Dietl, T. Ferromagnetic semiconductors. *Semicond. Sci. Technol.* **2002**, *17*, 377.

(4) Felser, C.; Fecher, G. H.; Balke, B. Spintronics: a challenge for materials science and solid-state chemistry. *Angew. Chem., Int. Ed.* **2007**, *46*, 668−699.

(5) Dietl, T. A ten-year perspective on dilute magnetic semiconductors and oxides. *Nat. Mater.* **2010**, *9*, 965−974.

(6) Dietl, T.; Ohno, H. Dilute ferromagnetic semiconductors: Physics and spintronic structures. *Rev. Mod. Phys.* **2014**, *86*, 187.

(7) Gong, C.; Li, L.; Li, Z.; Ji, H.; Stern, A.; Xia, Y.; Cao, T.; Bao, W.; Wang, C.; Wang, Y.; Qiu, Z. Q.; Cava, R. J.; Louie, S. G.; Xia, J.; Zhang, X. Discovery of intrinsic ferromagnetism in two-dimensional van der Waals crystals. *Nature* **2017**, *546*, 265−269.

(8) Huang, B.; Clark, G.; Navarro-Moratalla, E.; Klein, D. R.; Cheng, R.; Seyler, K. L.; Zhong, D.; Schmidgall, E.; McGuire, M. A.; Cobden, D. H.; Yao, W.; Xiao, D.; Jarillo-Herrero, P.; Xu, X. Layer-dependent ferromagnetism in a van der Waals crystal down to the monolayer limit. *Nature* **2017**, *546*, 270−273.

(9) Huang, B.; Clark, G.; Klein, D. R.; MacNeill, D.; Navarro-Moratalla, E.; Seyler, K. L.; Wilson, N.; McGuire, M. A.; Cobden, D. H.; Xiao, D.; Yao, W.; Jarillo-Herrero, P.; Xu, X. Electrical control of 2D magnetism in bilayer CrI3. *Nat. Nanotechnol.* **2018**, *13*, 544−548.

(10) Jiang, S.; Li, L.; Wang, Z.; Mak, K. F.; Shan, J. Controlling magnetism in 2D CrI_3 by electrostatic doping. *Nat. Nanotechnol.* **2018**, *13*, 549−553.

(11) Wang, Z.; Zhang, T.; Ding, M.; Dong, B.; Li, Y.; Chen, M.; Li, X.; Huang, J.; Wang, H.; Zhao, X.; Li, Y.; Li, D.; Jia, C.; Sun, L.; Guo, H.; Ye, Y.; Sun, D.; Chen, Y.; Yang, T.; Zhang, J.; Ono, S.; Han, Z.; Zhang, Z. Electric-field control of magnetism in a few-layered van der Waals ferromagnetic semiconductor. *Nat. Nanotechnol.* **2018**, *13*, 554−559.

(12) Klein, D. R.; MacNeill, D.; Lado, J. L.; Soriano, D.; Navarro-Moratalla, E.; Watanabe, K.; Taniguchi, T.; Manni, S.; Canfield, P.; Fernández-Rossier, J.; Jarillo-Herrero, P. Probing magnetism in 2D van der Waals crystalline insulators via electron tunneling. *Science* **2018**, *360*, 1218−1222.

(13) Seyler, K. L.; Zhong, D.; Klein, D. R.; Gao, S.; Zhang, X.; Huang, B.; Navarro-Moratalla, E.; Yang, L.; Cobden, D. H.; McGuire, M. A.; Yao, W.; Xiao, D.; Jarillo-Herrero, P.; Xu, X. Ligand-field helical luminescence in a 2D ferromagnetic insulator. *Nat. Phys.* **2018**, *14*, 277−281.

(14) Miao, N.; Xu, B.; Zhu, L.; Zhou, J.; Sun, Z. 2D Intrinsic Ferromagnets from van der Waals Antiferromagnets. *J. Am. Chem. Soc.* **2018**, *140*, 2417−2420.

(15) Li, X.; Yang, J. Realizing Two-Dimensional Magnetic Semiconductors with Enhanced Curie Temperature by Antiaromatic Ring Based Organometallic Frameworks. *J. Am. Chem. Soc.* **2019**, *141*, 109−112.

(16) Tsubokawa, I. On the magnetic properties of a $CrBr_3$ single crystal. *J. Phys. Soc. Jpn.* **1960**, *15*, 1664−1668.

(17) Matthias, B. T.; Bozorth, R. M.; Van Vleck, J. H. Ferromagnetic Interaction in EuO. *Phys. Rev. Lett.* **1961**, *7*, 160.

(18) Baltzer, P. K.; Lehmann, H. W.; Robbins, M. Insulating Ferromagnetic Spinels. *Phys. Rev. Lett.* **1965**, *15*, 493.

(19) Kimura, T.; Kawamoto, S.; Yamada, I.; Azuma, M.; Takano, M.; Tokura, Y. Magnetocapacitance effect in multiferroic $BiMnO_3$. *Phys. Rev. B: Condens. Matter Mater. Phys.* **2003**, *67*, 180401.

(20) Ando, K. Seeking Room-Temperature Ferromagnetic Semiconductors. *Science* **2006**, *312*, 1883−1885.

(21) Olejník, K.; Owen, M. H. S.; Novák, V.; Mašek, J.; Irvine, A. C.; Wunderlich, J.; Jungwirth, T. Enhanced annealing, high Curie temperature, and low-voltage gating in (Ga,Mn)As: A surface oxide control study. *Phys. Rev. B: Condens. Matter Mater. Phys.* **2008**, *78*, 054403.

(22) Katsnelson, M. I.; Irkhin, V. Yu.; Chioncel, L.; Lichtenstein, A. I.; de Groot, R. A. Half-metallic ferromagnets: From band structure to many-body effects. *Rev. Mod. Phys.* **2008**, *80*, 315.

(23) Anderson, P. W. Antiferromagnetism. Theory of Superexchange Interaction. *Phys. Rev.* **1950**, *79*, 350.

(24) Goodenough, J. B. Theory of the Role of Covalence in the Perovskite-Type Manganites [La, *M*(II)]MnO_3. *Phys. Rev.* **1955**, *100*, 564.

(25) Kanamori, J. Superexchange interaction of electron and symmetry properties of electron orbitals. *J. Phys. Chem. Solids* **1959**, *10*, 87−98.

(26) Huang, C.; Feng, J.; Wu, F.; Ahmed, D.; Huang, B.; Xiang, H.; Deng, K.; Kan, E. Toward Intrinsic Room-temperature Ferromagnetism in Two-dimensional Semiconductors. *J. Am. Chem. Soc.* **2018**, *140*, 11519−11525.

(27) Slater, J. C.; Koster, G. F. Simplified LCAO Method for the Periodic Potential Problem. *Phys. Rev.* **1954**, *94*, 1498.

(28) Silva-Guillén, J. Á.; San-Jose, P.; Roldán, R. Electronic Band Structure of Transition Metal Dichalcogenides from Ab Initio and Slater−Koster Tight-Binding Model. *Appl. Sci.* **2016**, *6*, 284.

(29) Sanyal, B.; Bergqvist, L.; Eriksson, O. Ferromagnetic materials in the zinc-blende structure. *Phys. Rev. B: Condens. Matter Mater. Phys.* **2003**, *68*, 054417.

(30) Gao, G. Y.; Yao, K. L.; Şaşıoğlu, E.; Sandratskii, L. M.; Liu, Z. L.; Jiang, J. L. Half-metallic ferromagnetism in zinc-blende CaC, SrC, and BaC from first principles. *Phys. Rev. B: Condens. Matter Mater. Phys.* **2007**, *75*, 174442.
(31) McGuire, M. A.; Dixit, H.; Cooper, V. R.; Sales, B. C. Coupling of Crystal Structure and Magnetism in the Layered, Ferromagnetic Insulator CrI_3. *Chem. Mater.* **2015**, *27*, 612−620.
(32) Wang, Y.; Lv, J.; Zhu, L.; Ma, Y. Crystal structure prediction via particle-swarm optimization. *Phys. Rev. B: Condens. Matter Mater. Phys.* **2010**, *82*, 094116.
(33) Wang, Y.; Lv, J.; Zhu, L.; Ma, Y. CALYPSO: A method for crystal structure prediction. *Comput. Phys. Commun.* **2012**, *183*, 2063−2070.
(34) Etgens, V. H.; de Camargo, P. C.; Eddrief, M.; Mattana, R.; George, J. M.; Garreau, Y. Structure of Ferromagnetic CrAs Epilayers Grown on GaAs(001). *Phys. Rev. Lett.* **2004**, *92*, 167205.
(35) Giebultowicz, T. M.; Kłosowski, P.; Samarth, N.; Luo, H.; Furdyna, J. K.; Rhyne, J. J. Neutron-diffraction studies of zinc-blende MnTe epitaxial films and MnTe/ZnTe superlattices: The effect of strain and dilution on a strongly frustrated fcc antiferromagnet. *Phys. Rev. B: Condens. Matter Mater. Phys.* **1993**, *48*, 12817.

DOI: 10.1021/jacs.9b06452
J. Am. Chem. Soc. 2019, 141, 12413−12418